Focused helium ion beam deposited low resistivity cobalt metal lines with 10 nm resolution: implications for advanced circuit editing

H. Wu · L. A. Stern · D. Xia · D. Ferranti ·
B. Thompson · K. L. Klein · C. M. Gonzalez ·
P. D. Rack

Abstract Helium ion beam induced cobalt nanowire deposition using dicobalt octacarbonyl ($Co_2(CO)_8$) as a precursor is described. 10 nm wide metal lines were fabricated with good repeatability and extremely high purity. The metal lines were deposited on electrical test structures to determine the nanowire resistivity and contact resistance. Measurements reveal that these metal lines have 50–100 $\mu\Omega$-cm resistivity. The contact resistance of a Co line on a gold pad is 15 Ω with a 0.14×1.4 μm contact area. The resulting metal deposit size was determined by helium ion microscopy (HIM) because of its high imaging resolution, and further characterized by high resolution transmission electron microscopy (HR-TEM) and electron energy-loss spectroscopy (EELS). HR-TEM images reveal that these metal lines are composed of 6 ± 2 nm cobalt crystallite grains; and EELS analysis shows that no measurable carbon signal was observed. Single-line and multiple-line patterns were prepared to examine proximity effects around the metal line depositions. Both HIM imaging and electrical measurements of the patterns verify that the collateral proximity deposition between individual lines can be minimized. Finally, factors determining the ultimate line width achievable with the He ion beam are discussed.

1 Introduction

The dimensions of integrated circuits, data storage and biological/medical devices continue to shrink, consequently, there is a constant need to improve existing process technologies, as well as develop new materials, innovative device structure design and novel fabrication methods. Ga-focused ion beams (Ga-FIB) and electron beams (e-beam) have been used historically for direct deposit or removal of nano- and micro-scale features for circuit edit and repair in the prototyping stage of the design process [1–3]. Using typically organo-metallic compounds as the precursor gas, Ga-FIB and e-beam can induce the dissociation of the precursor, resulting in the (partial) volatilization of the carbonaceous components and the condensation of the metal (and some residual carbon) component in the beam interaction region [4–6].

The geometric resolution obtained in milling and deposition processes by ion [7, 8] and e-beam [9] is dependent on the ion/electron beam profile and the lateral spreading of the beam energy on the substrate caused by collision cascades. To deposit very narrow (sub-10 nm) metal lines, one must optimize the beam profile and minimize the lateral energy spread. The primary electron beams used for focused e-beam induced deposition (FE-BID) in a scanning electron microscope typically have an energy of 1–30 keV and a beam current of 1 pA–20 nA, which can be focused to about a 2–100 nm spot size depending on the source and beam settings; greater beam current normally has a larger spot size. The Ga-FIB has a few nanometer spot size at 1–50 kV beam energy. The new

H. Wu (✉) · L. A. Stern · D. Xia · D. Ferranti · B. Thompson
Carl Zeiss Microscopy LLC, One Corporation Way, Peabody,
MA 01960, USA
e-mail: huimeng.wu@zeiss.com

K. L. Klein
The University of the District of Columbia, 4200 Connecticut
Ave, NW, Washington, DC 20008, USA

C. M. Gonzalez · P. D. Rack
The University of Tennessee, 603 Dougherty Hall, Knoxville,
TN 37996-2200, USA

Zeiss Orion gas field ion source (GFIS) column provides both helium and neon ion beams, with an ultimately smaller probe size (spot size for HeIM is 0.5 nm; for NeIM is 1.9 nm) relative to electron beam and Ga-FIB, as well as a 10 times lower energy spread (<1 eV FWHM) than a liquid metal ion source (LMIS) [10–12]. Energy spread causes chromatic aberration and widens the beam tail of a LMIS beam. The nearly monochromatic GFIS has a beam profile with much less beam tail contribution. The capability of Orion to fabricate sub 10 nm patterns at high densities provides a unique solution for direct precise maskless and resistless patterned fabrication.

In addition to the geometric resolution requirements, the properties of deposited materials are critical, and depend on the purity and nanostructure of the deposits. For most organometallic precursors, the deposited material is a mixture of the desired metal, carbon, and oxygen from the organic components in the precursor gas. Normally, Ga-FIB induced metal deposits have better electrical properties because of their higher metal percentage and gallium implantation relative to FEBID. Also Ga-FIB induced metal deposits have slightly larger grains sizes and better crystalline structures relative to electron beam deposits. Platinum and tungsten are the most common choices for the metal of the precursor gases in FIB or FEBID, and the deposition properties of both have been extensively characterized in previous works. For example, with trimethyl (methylcyclopentadienyl)platinum(IV) (MeCpPtMe$_3$) as the precursor, it was reported that Ga-FIB induced Pt deposits have 46 % Pt, 24 % C, 28 % Ga, and 2 % O, with a measured resistivity between 70 and 700 $\mu\Omega$ cm[13]. Such relatively low resistivity is partially attributed to the large amount of Ga implantation from the ion beam. For FEBID from the same precursor, the deposits have typically 15–25 at.% Pt [14]. The abundant amorphous carbon and poor crystalline Pt structure result in a resistivity on the order of 10^7 $\mu\Omega$ cm [15]. Post-process treatment (such as laser, thermal annealing, or current annealing) can help to improve the metal content and subsequently lower the resistivity of e-beam deposited Pt–C. Two methods have recently been described in situ to improve the deposited Pt quality: (1) post-electron beam exposure [16, 17] and (2) laser assisted electron beam induced deposition [15].

The introduction of the GFIS microscope has created significant interest for nanoscale imaging [18–22], lithography [23, 24], and nanoscale synthesis [23, 25–31]. While most of the work has revolved around the helium ion source, there have been reports on neon GFIS regarding stability, imaging and nanofabrication [32, 33]. We reported recently the helium and neon ion beams induced nanoscale synthesis of platinum nanowires with MeCpPtMe$_3$ as the precursor [34].The mass difference between He and Ne ions results in significant differences in the deposits. The He$^+$ beam deposited material composition has smaller platinum grain size and much larger resistivity (minimum: 3×10^4 $\mu\Omega$ cm) than Ne$^+$ deposited material (minimum resistivity: 600 $\mu\Omega$ cm). Monte-Carlo ion–solid simulations show that the neon energy density deposited during growth is much greater due to the smaller ion range and is dominated by nuclear stopping relative to helium which has a larger range and is dominated by electronic stopping [34].

To determine the ultimate line width possible for the GFIS microscope (using either He or Ne ion beam induced processes) and improve the deposition quality, we have explored new metal precursors and optimized the deposition conditions. The choice of metal precursors for nanofabrication in circuit edit is determined by many factors, namely minimizing the deposit resistivity, low contact resistance, proximity deposition and feature size, while maintaining chemical and thermal stability of the interface region and main deposits, high purity, etc. Besides Pt and W deposits, many other metals, such as gold, iron, and cobalt have been investigated [35–37]. For example, e-beam induced cobalt deposition using dicobalt octacarbonyl [5, 38–40] and electrically conductive lines for Hall devices [41]. The minimum resistivity of deposited free space arches is 159 $\mu\Omega$ cm with an 80 % Co content using a 10.7 nA e-beam current. In another report, using a 2 nA e-beam current, Co nanowires were deposited on a 4-probe structure. Co content as high as 95 % was obtained and the resistivity was $\sim$40 $\mu\Omega$-cm [42]. In both cases, the Co content has been found to correlate with the e-beam current used for the deposition. High e-beam current resulted in high metallic content deposits, which was explained by a thermal effect and the catalytic decomposition of the cobalt precursor. However, high beam current also results in a larger spot size (several nanometers) and poor beam profile, which limits the ability to fabricate small feature sizes <50 nm. It was reported that the adsorption of the precursor might already result in partial dissociation or clustering to bigger Co–Co bond containing units, resulting in large halos or proximal deposition around the deposits. So far, few Ga-FIB induced Co deposits have been reported. This may be because of the large sputter rate of the Ga ion beam competing with deposition.

In this work, helium ion beam induced cobalt nanowire deposition using Co$_2$(CO)$_8$ as a precursor is described. The metal lines were deposited on electrical test structures for electrical measurements to calculate their resistivity and contact resistance. The resulting metal deposits were directly inspected for their geometric dimensions by helium ion microscopy (HIM) because of its high imaging resolution, and further characterized by high resolution transmission electron microscopy (HR-TEM) and electron energy-loss spectroscopy (EELS). Single-line and multiple-line patterns

were prepared to examine proximity effects around the metal line deposits. Both HIM imaging and electrical measurements of the patterns verified that the collateral deposition between individual lines can be minimized. Finally, factors determining ultimate line width using He ion beam are discussed.

2 Experimental methods

2.1 Gas field ion beam induced deposition

All cobalt nanostructures were deposited using a Zeiss OrionPlus^{TM} microscope (Fig. 1) with a GFIS column. Dicobalt octacarbonyl ($Co_2(CO)_8$) was used as a precursor delivered by an Omniprobe gas injection system (GIS). The precursor was cooled to 15 °C and the N_2 carrier gas was at 25 °C. The GIS nozzle end was about 70 μm above the sample at an angle of approximately 30° relative to the sample surface. The chamber pressure before and after opening the GIS valve was 5.0×10^{-7} to 6×10^{-6} Torr, respectively. A Fibics NPVE pattern generator was used to control the scanning parameters. Cobalt lines were deposited on a nanofabricated test wafer. Two kinds of structures on this wafer were utilized: a 4 point probe test structure (4-ppt) and a contact resistance test structure (CRT). The layouts of 4-ppt and CRT are shown in Fig. 2a and b respectively. Figure 2c and d are higher magnifications of the yellowdashed areas highlighted in Fig. 2a and b. The gold electrode fingers are ∼100 nm thick (on 10 nm Cr adhesion layer) on a 500 nm thermal oxide on a silicon substrate. The central separated gap (G) is ∼1.6 μm in a 4-ppt, which is labeled in Fig. 2c. The separated gaps in CRT from bottom to top are: 0.6, 1.6, 2.6, 3.6, 4.6, and 5.6 μm.

All deposits were produced with the helium ion beam and no post-annealing process or post-deposition cleanup process was performed. By optimizing the ratio of precursor gas to carrier gas and beam conditions, we minimized proximal deposition around the Co deposition. A beam energy of 35 keV and beam current of 1.5 pA, pixel spacing of 1–5 nm, dwell time of 0.5 μs, serpentine scan style with a 100 μs refresh time were set as the standard beam conditions for cobalt deposition. To deposit relatively large feature cobalt lines (larger than 25 nm), a 20 μm or 10 μm beam limiting aperture was used. A 5 μm beam limiting aperture with beam current of 0.8 pA was used to obtain narrower cobalt lines. A smaller aperture can yield a smaller ion beam probe, thus the usage of a smaller aperture can deposit narrower lines but requires longer process time for comparable thickness. To deposit 10 nm Co lines, a single line scan mode was used.

Using the above deposition conditions, single line and multiple-line patterns with various line widths were deposited on 4-ppt structures. A single line with a 140 nm width was deposited on the CRT structure. The samples for

Fig. 1 A photograph of the Zeiss OrionPlus^{TM} microscope used for this work

Fig. 2 Helium ion beam microscope (HIM) images of 4-point probe test structure (4-ppt, **a** and **c**) and contact resistance test structure (CRT, **b** and **d**). The central separated gap of 4-ppt is labeled as "G" ($\sim 1.6\ \mu m$), shown in Fig. 2c. The Au pads are labeled as 1–4. Current is applied on pads 1 and 4 connecting the two outside probes and voltage is measured on pads 2 and 3 connecting the central two probes. The separated gaps in the CRT structure from *bottom* to *top* (labeled as 1–6 in Fig. 2d) are: 0.6, 1.6, 2.6, 3.6, 4.6, and 5.6 μm, respectively. The *metal lines* will be deposited across the gold fingers
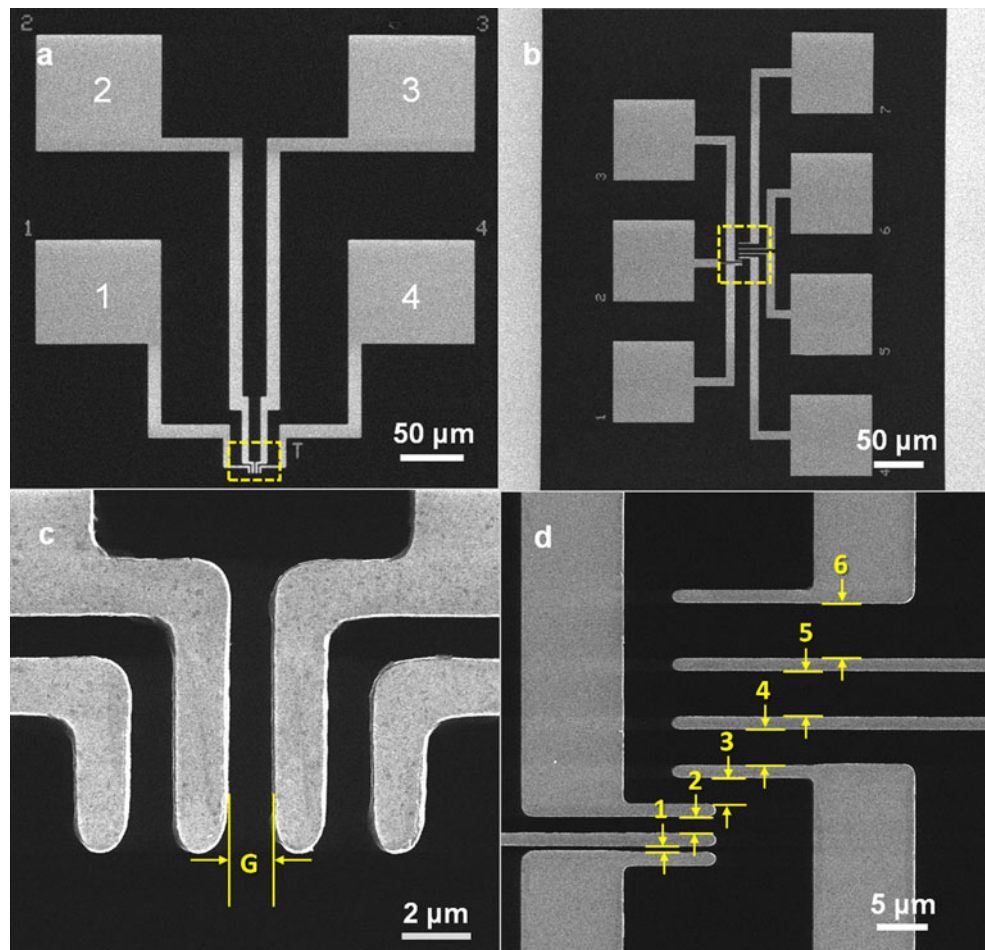
transmission electron microscopy (TEM) and EELS measurements were prepared by depositing $\sim 7.5\ \mu m$ long by ~ 500 nm wide rectangular boxes on a 30 nm thick Si_3N_4 membrane using the same beam conditions.

2.2 Electrical measurements

Electrical properties were determined by depositing cobalt lines on 4-ppt structures and CRT structures on a test chip. Room temperature electrical measurements were performed using a Signatone probe station equipped with a Keithley 4200 with a pre-amplifier. The standard four probe measurements for a 30 nm wide Co line were made by forcing a source current from 0 to 90 μA with a 500 nA increment between the outer two probes and measuring the voltage drop between the inner two probes. The Co deposits were imaged by HIM, including a top view and a 45° tilted view to determine the cross-sectional area and specific gap dimensions for resistivity calculations.

The two probe measurements were performed by forcing a source current from 0 to 90 μA with a 500 nA increment between the two probes to calculate the contact resistance.

2.3 Transmission electron microscopy (TEM) imaging and electron energy loss spectroscopy (EELS)

To further characterize the depositions, both TEM and EELS were performed. TEM and EELS experiments were performed using a Philips/FEI CM 300 TEM equipped with a Gatan post-column energy filter (GIF). The TEM data were collected in bright-field mode at 300 keV. Zero-loss energy filtering with a 10 eV slit was used to improve image quality. EELS was performed at a 300 keV using a 0.5 eV dispersion with a 30 μm objective aperture.

3 Results and discussions

The He ion beam induced cobalt line depositions with various line widths on 4 point probe test structures (4-ppt) are shown in Fig. 3. Figure 3a is a HIM image of a single Co line with 30 nm width and 9 μm length on a 4-ppt. Although the line is thin (only 30 nm thickness), the step coverage of the Co line is good, as shown in the inset of Fig. 3a. The line width and length can be directly adjusted by changing the pattern size. The thickness of the line can

Fig. 3 HIM images of He ion beam induced single cobalt line depositions with various line widths on 4 ppt structures: 50 nm (**b**), 30 nm (**a** and **c**) and 10 nm (**d**). **a** shows a Co line with 30 nm width and 10 μm length on 4ppt. The *inset* shows the good step coverage. **b–d** show higher magnification HIM images of 50 nm, 30 nm and 10 nm Co lines. The *insets* in **b** and **c** are 3D schematic drawings of Co lines
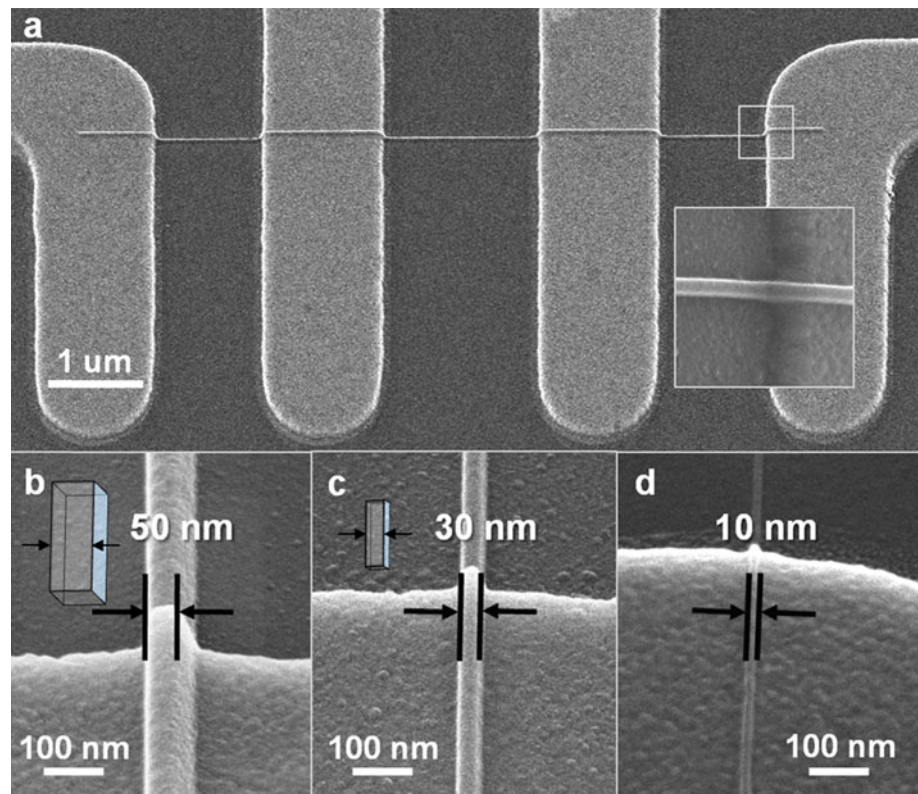
be modified by varying the dose per area for the deposition. Figure 3 b–d show higher magnification HIM images of 50, 30 and 10 nm Co lines, respectively.

It is noteworthy that all single metal lines shown in Fig. 3 were deposited by HIM without any additional cleaning process and/or post-annealing. The high magnification HIM images clearly show that these metal line deposits have well-defined contours and little proximity deposition (halo effect) around the deposits. Because of a minimal amount of collateral deposition around the deposits and the very narrow line width, we are able to make very dense metal line arrays. Figure 4a is a 4 line pattern with a 25 nm half pitch. The high resolution HIM images of this deposition with a 45° tilt angle at different rotations are shown in Fig. 4b and c.

As mentioned before, spontaneous dissociation or backscattered ions or secondary electron induced dissociation of $Co_2(CO)_8$ can cause a large halo or proximity deposition around the deposits. The rate of dissociation of the precursor is dependent on the beam profile and the amount of the precursor molecule on the substrate surface [41, 43]. For our Co deposition, we found by simply increasing the carrier gas amount to dilute the precursor gas concentration, we can significantly reduce the collateral deposition area around the deposits (shown in Fig. 5a, b). These two single Co lines were deposited using similar deposition conditions except for the amount of carrier gas.

Figure 5a was made at the ratio of carrier gas to precursor gas of 1:1, and Fig. 5b was at the ratio of 4:1. The halo area can be further minimized by using a smaller beam limiting aperture and optimizing beam alignment. The results of the optimization are shown previously in Figs. 3 and 4. We are able to fabricate 4 Co lines with a 25 nm half pitch, without significant overspray based on the HIM images. Notably, all lines have good step coverage on the gold fingers.

These results are very important for circuit edit applications in the semiconductor industry. Collateral deposition around the deposits can significantly widen the dimension and cause current leakage. Therefore, eliminating proximity or halo deposition has become a well known challenge for FIB induced deposition. To this end, post-deposition "clean" processes (such as Ga ion sputter with or without XeF_2) for Ga-FIB induced deposition is common. FEBID can reduce the deposition size (50–100 nm) and also minimize halos, but typically e-beam deposition requires post-processing for high-purity deposits (for example by laser, electrical current or local thermal heating). Because of the heavier mass of He and Ne ions relative to e-beam, and the well-defined beam profile and smaller probe size than a Ga ion beam, the GFIS microscope with both He and Ne ion beams is an ideal tool to fabricate high-purity sub-10 nm features.

Figure 6 shows typical I–V curves for single cobalt line and multiple lines, respectively. The deposition conditions,

Fig. 4 HIM images of a 4 line pattern with a 25 nm half pitch. **a** *top view*; **b** and **c** are 45° *tiltled angles* high resolution HIM images of this deposit with different rotations
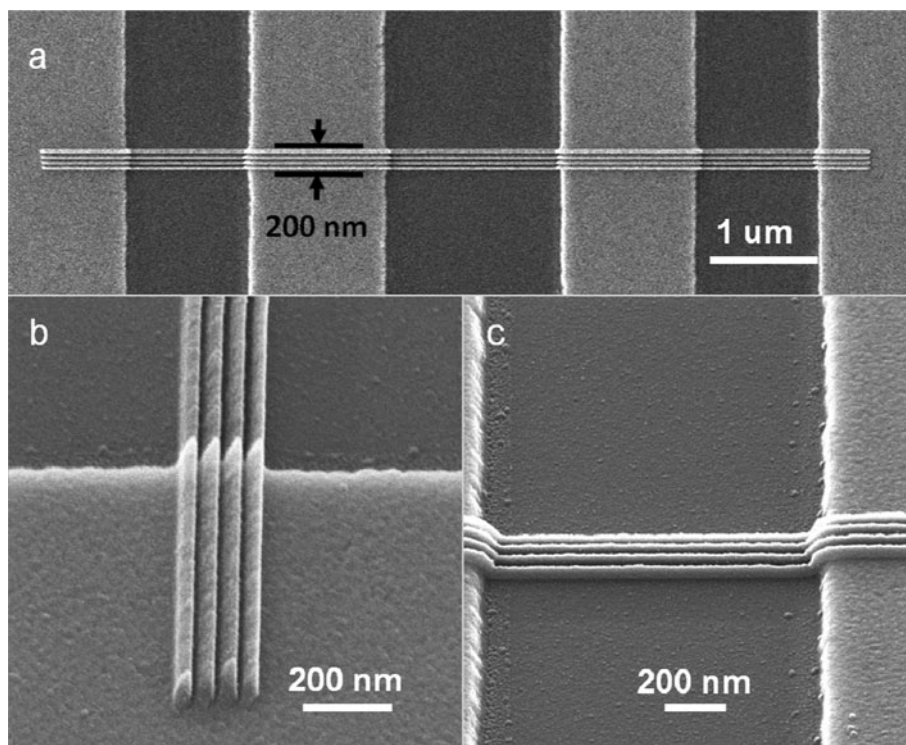
geometry size and electrical measurement results of Co lines are summarized in Table 1. The resistivity (ρ) is calculated according to Eq. 1:

$$\rho = \frac{R_m \cdot A_m}{G} \tag{1}$$

Here R_m is the metal line resistance, A_m is the cross section area of the metal line, and G is the gap distance between two gold fingers. Here we assume the cross-section of metal deposits is rectangular, then $A_m = w \times t$ (*w*: width of metal line; *t*: thickness of metal line).

The resistivities of the first three single Co lines are 64, 76 and 76 μΩ-cm respectively, which is ten times higher than bulk Co resistivity (6.24 μΩ-cm). The resistivity of the 10 nm Co line (116 μΩ-cm) is slightly larger than the others, which may be caused by the imprecision of the geometry measurement or the dose effect [44]. However, to our knowledge, at such a small geometry, this resistivity is still the lowest result reported to date. The electrical measurement result of multiple-line patterns is also summarized in Table 1. The average resistivity of multiple line patterns is 68 μΩ-cm, which is very close to the average resistivity of single lines. No significant reduction of the resistivity for the 4 line pattern suggests that the proximal deposition between the deposit lines is minimal (Table 2).

One concern using cobalt to do rewire or any nanofabrication application is the cobalt stability. To address this

Fig. 5 HIM images of single Co line on 4-ppt at carrier gas to precursor gas ratio of (**a**) 1:1 and (**b**) 4:1. **a** shows a *top view* image and **b** a 45° *tilted* image
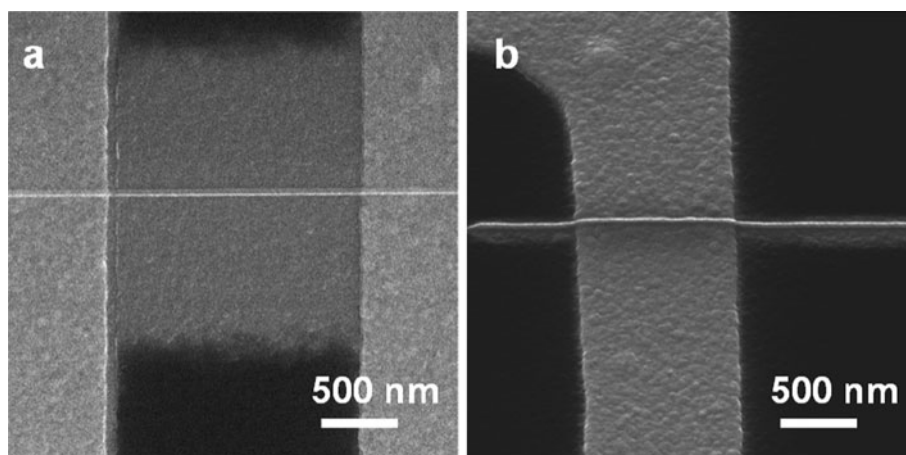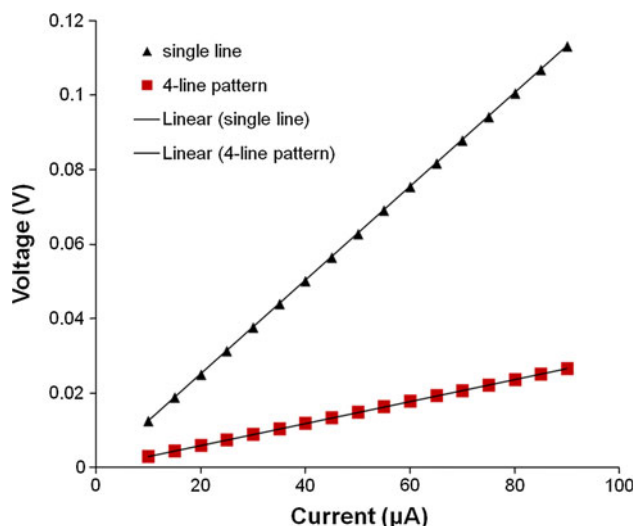
Fig. 6 Typical I–V curves for single cobalt line (*triangles*) and multiple lines (*squares*). The *lines* are linear fittings (Color figure online)

concern, we re-measured the Co lines after 4 months, and observed less than 5 % change in the resistance.

For circuit repair and rewiring applications, it is important to have good electrical contact between the deposited metal line and the underlying metal. Thus, we designed a new contact resistance test structure, as shown in Fig. 2b and d. Figure 7a shows a HIM image of a cobalt line deposited across the CRT test structure. Higher magnification of the wire is shown in Fig. 7b. The resistance (R)® cobalt line contacts on the gold electrodes as a function of the 2 point probe length is plotted in Fig. 7c. The total resistance between gold electrode pads is the sum of the cobalt line resistance and the resistance from the contacts to the gold electrodes (assuming the gold line resistance is negligible). Thus we have following Eq. 2:

$$R_{total} = R_m + 2R_c = \frac{\rho \cdot G}{A_m} + 2R_c \tag{2}$$

Here ρ is the resistivity of the deposited metal line, R_m is the metal line resistance, G is the gap distance (or length of metal line) between two gold pads and A_m is the cross section area of the metal line. Since all the contacts were deposited at the same time with the same contact area (A_c), R_c is assumed to be constant. Therefore, a linear regression

Table 2 Two probe measurements of a Co line on contact resistance test structure

Gap distance (nm)	R (Ω)
1,600	141
2,600	211
3,600	283
4,600	415
5,600	426

analysis was performed on the data and the best-fit line determined. As the distance between the contact pads goes to zero, the y intercept of the best-fit line will correspond to $2R_c$, and the slope of the linear fit is ρ/A_m, which can be multiplied by A_m to yield ρ. From Fig. 7c, we calculated a contact resistance R_c of 15 Ω for a 140 nm wide Co line on 1.4 μm wide gold electrode finger (or a specific contact resistivity of 0.03 μΩ-cm^2) and a corresponding resistivity ρ of 59 μΩ-cm. For comparison, bulk material the specific contact resistivity of metal on metal is <0.01 μΩ-cm^2 and metal on doped silicon is in the range of 10–0.1 μΩ-cm^2. Recently, it was shown that Ga-FIB deposited Pt and W on heavily doped silicon had a contact resistivity of 1×10^5 and 1×10^4 μΩ-cm^2 [45] Similarly, Pt deposited onto ZnO nanowires revealed a specific contact resistivity of 15 μΩ-cm^2 [46]. Finally, optimized Ga-FIB deposited tungsten on aluminum contacts had a contact resistivity of 1.6 μΩ-cm^2 [47].

To further characterize the depositions, both TEM and EELS were performed. Figure 8a and b are low magnification bright-field TEM images of a Co deposit on a 30 nm thick Si_3N_4 membrane. Figure 8c is a higher magnification TEM image of the Co deposit. It is clearly shown that the Co deposit is composed of nanoscale cobalt grains. Statistical analysis of Co grain size in the deposition reveals that grain size is 6 (±2) nm. The grain size of e-beam induced Co deposition from the same precursor has been reported 1–2 nm [48]. He ion beam induced Co deposits have a relatively larger grain size. The spacing of lattice fringe measured from HRTEM image (see Fig. 8c) is 2.0 Å, which corresponds to (002) lattice spacing of *hcp* cobalt crystals.

Table 1 Summary of size and electrical measurement of single-lines and multiple lines of Co deposits

Sample ID	Description	E (keV)	I (pA)	Width (nm)	Thickness (nm)	Gap (nm)	R (Ω)	ρ (Ω cm)
1	Single line	35	1.3	31	30	1,600	1,100	64
2	Single line	35	1.3	31	30	1,600	1,300	76
3	Single line	35	1.3	50	35	1,600	699	76
4	Single line	35	1.3	10	6	1,600	31,000	116
5	4 line with 50 nm pitch	35	1.4	28	33	1,600	295	68

Fig. 7 A HIM image of cobalt line across the CRT structure (**a**) and a high magnification HIM image with a 45° tilt angle (**b**). **c** A plot of the resistance of cobalt line contacts on the gold electrodes as a function of the 2 point probe length
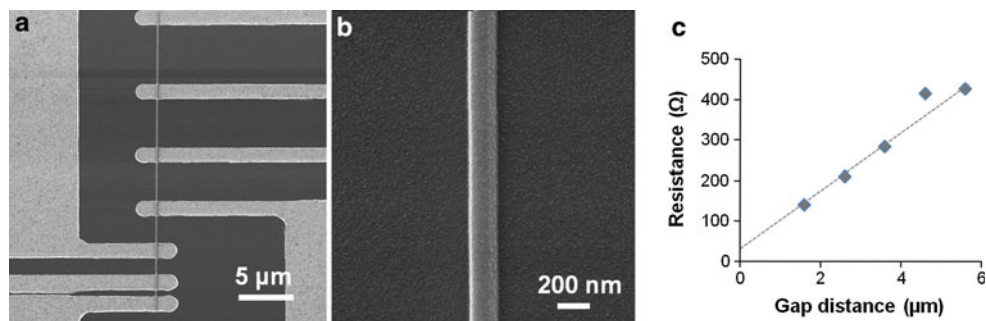

Fig. 8 TEM images of a Co deposit on a 30 nm thickness Si₃N₄ membrane. **a** and **b** are bright-field TEM images at different magnifications. **c** is an even higher magnification TEM image of the Co deposit. It is clearly shown that Co deposit is composed of ∼6 nm nanocrystallites. **d** is a HRTEM image of the Co deposit. The lattice fringe measured is 2.0 Å
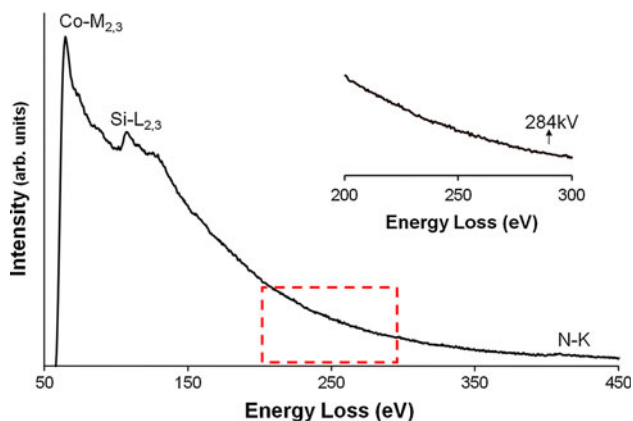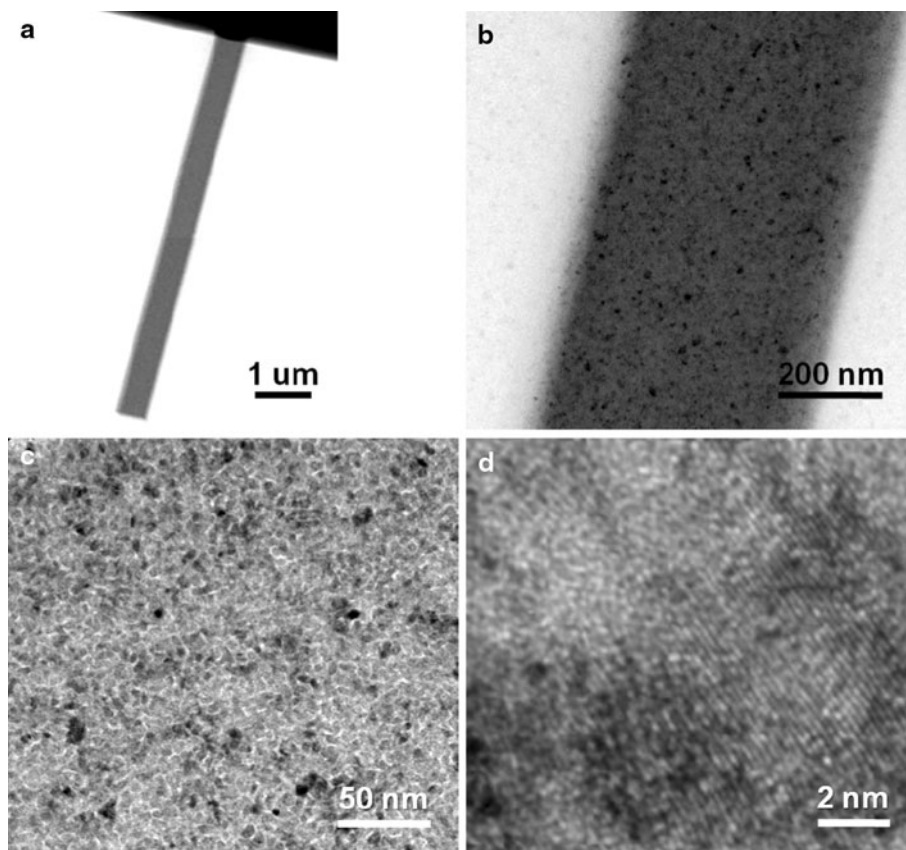

Fig. 9 Background-subtracted EELS spectra of the Co deposits. The *inset* shows the enlarged spectrum from 200 to 300 eV to verify the absence of a measurable C–K edge at 284 eV

To estimate the carbon content of the helium ion beam induced deposits, EELS was used instead of EDX, because it is more sensitive to light elements and there is little peak overlap with the elements involved. The 0–450 eV region is convenient for mapping out cobalt (Co-$M_{2,3}$ edge with threshold at 60 eV) and carbon (C–K edge at 284 eV). Background-subtracted EELS spectra are shown in Fig. 9. The Co-$M_{2,3}$ absorption edge is clearly shown at 60 eV, but no measurable carbon signal was observed for any of the Co deposits. The silicon L1,2 edge at 99 eV results from the silicon nitride membrane. The minimum detectable mass fraction for EELS has been reported on the order of a few atomic percent [49]. Thus we attribute the low resistivity of Co lines deposited by the He ion beam to the high cobalt purity and large grain size.

4 Conclusions

In summary, we have demonstrated the feasibility of depositing high-quality Co lines by helium ion beam with metallic conduction within an order of magnitude of the bulk value. This is in good agreement with EELS measurements, negligible carbonaceous contamination, and HRTEM images, which show relatively larger grain sizes than that of FEBID-Co nanowires. Because of the extremely small spot size of the helium beam, we are able to deposit as small as 10 nm wide single or multiple Co lines at high densities with almost no overspray around the deposits. These results, together with the high flexibility platform of the Orion confirm that this specific technique represents an attractive approach for fabricating state of the art nanoscale structures with high purity.

References

1. L.R. Harriott, A. Wagner, F. Fritz, J. Vac. Sci. Technol. B **4**, 181 (1986)
2. T. Liang, E. Frendberg, B. Lieberman, A. Stivers, J. Vac. Sci. Technol. B **23**, 3101 (2005)
3. M.G. Lassiter, T. Liang, P.D. Rack, J. Vac. Sci. Technol. B **26**, 963 (208)
4. A.N. Broers, W.W. Molzen, J.J. Cuomo, N.D. Wittels, Appl. Phys. Lett. **29**, 596 (1976)
5. Y.M. Lau, P.C. Chee, J.T.L. Thong, V. Ng, J. Vac. Sci. Technol. A **20**, 1295 (2002)
6. T. Bret, I. Utke, P. Hoffmann, M. Abourida, P. Doppelt, Microelectron. Eng. **83**, 1482 (2006)
7. D.A. Smith, D.C. Joy, P.D. Rack, Nanotechnology **21**, 175302 (2010)
8. R. Ramachandra, B. Griffin, D. Joy, Ultramicroscopy **109**, 748 (2009)
9. D.A. Smith, J.D. Fowlkes, P.D. Rack, Small **4**, 1382 (2008)
10. V.N. Tondare, J. Vac. Sci. Technol. A **23**, 1498 (2005)
11. B.W. Ward, J.A. Notte, N.P. Economou, J. Vac. Sci. Technol. B **24**, 2871 (2006)
12. J. Orloff, R. Beach (eds.), *Handbook of Charged Particle Optics* (CRC Press, Boca Raton, 1997)
13. T. Tao, J. Ro, J. Melngailis, Z. Xue, H.D. Kaesz, J. Vac. Sci. Technol. B **8**, 1826 (1990)
14. O. Yavas, C. Ochiai, M. Takai, Y.K. Park, C. Lehrer, S. Lipp, L. Frey, H. Ryssel, A. Hosono, S. Okuda, J. Vac. Sci. Technol. B **18**, 976 (2000)
15. N.A. Roberts, J.D. Fowlkes, G.A. Magel, P.D. Rack, Nanoscale **5**, 408 (2013)
16. F. Porrati, R. Sachser, C. H. Schwalb, A. S. Frangakis, M. Huth, J. Appl. Phys. **109**, 063715 (2011)
17. H. Plank, G. Kothleitner, F. Hofer, S. G. Michelitsch, C. Gspan, A. Hohenau, J. R. Krenn, J. Vac. Sci. Technol. B, **29**, 051801 (2011)
18. M.T. Postek, A.E. Vladar, Scanning **30**, 457 (2008)
19. D.C. Bell, Microsc Microanal **15**, 147 (2009)
20. L. Scipioni, C.A. Sanford, J. Notte, B. Thompson, S. McVey, J. Vac. Sci. Technol. B **27**, 3250 (2009)
21. J.A. Notte, Micros Today **20**, 16 (2012)
22. D.C. Joy, Micros Today **20**, 10 (2012)
23. P.F.A. Alkemade, E.M. Koster, E. van Veldhoven, D.J. Maas, Scanning **34**, 90 (2012)
24. D. Winston, J. Ferrera, L. Battistella, A.E. Vladar, K.K. Berggren, Scanning **34**, 121 (2012)
25. P. F. A. Alkemade, H. Miro, E. van Veldhoven, D. J. Maas, D. A. Smith, P. D. Rack, J. Vac. Sci. Technol., B, **29**, 06FG05 (2011)
26. C.A. Sanford, L. Stern, L. Barriss, L. Farkas, M. DiManna, R. Mello, D.J. Maas, P.F.A. Alkemade, J. Vac. Sci. Technol. B **27**, 2660 (2009)
27. P. Chen, E. van Veldhoven, C.A. Sanford, H.W.M. Salemink, D.J. Maas, D.A. Smith, P.D. Rack, P.F.A. Alkemade, Nanotechnology **21**, 455302 (2010)
28. P. Chen, H.W.M. Salemink, P.F.A. Alkemade, J. Vac. Sci. Technol. B **27**, 1838 (2009)
29. Y. Drezner, Y. Greenzweig, D. Fishman, E. van Veldhoven, D.J. Maas, A. Raveh, R.H. Livengood, J. Vac. Sci. Technol. B **30**, 041210 (2012)
30. P. F. A. Alkemade, P. Chen, E. van Veldhoven, D. Maas, J. Vac. Sci. Technol., B, **28**, C6f22 (2010)
31. Rajendra Timilsina, D.A. Smith, P.D. Rack, Nanotechnology **24**, 115302 (2012)
32. R.H. Livengood, S.D. Tan, R. Hallstein, J. Notte, S. McVey, F.H.M. Faridur Rahman, Nucl. Instrum. Methods A **645**, 136 (2011)
33. F.H.M. Rahman, S. McVey, L. Farkas, J.A. Notte, S.D. Tan, R.H. Livengood, Scanning **34**, 129 (2012)
34. H.M. Wu, L. Stern, J.H. Chen, M. Huth, C.H. Schwalb, H. Winhold, F. Porrati, C. Gonzalez, R. Timilsina, R.D. Rack, Nanotechnology **24**, 175302 (2013)
35. I. Utke, P. Hoffmann, J. Melngailis, J. Vac. Sci. Technol. B **26**, 1197 (2008)
36. W.F. van Dorp, C.W. Hagen, J. Appl. Phys. **104**, 081301 (2008)
37. S.J. Randolph, J.D. Fowlkes, P.D. Rack, Crit. Rev. Solid State Mater. Sci. **31**, 55 (2006)
38. L.M. Belova, O. Hellwig, E. Dobisz, E.D. Dahlberg, Rev. Sci. Instrum. **83**, 093711 (2012)
39. I. Utke, F. Cicoira, G. Jaenchen, P. Hoffmann, L. Scandella, B. Dwir, E. Kapon, D. Laub, P. Buffat, N. Xanthopoulos, H. Mathieu, J. Mat. Res. Soc. Symp. Proc. **706**, Z9.24.1, (2002)
40. I. Utke, P. Hoffmann, R. Berger, L. Scandella, Appl. Phys. Lett. **80**, 4792 (2002)
41. G. Boero, I. Utke, T. Bret, N. Quack, M. Todorova, S. Mouaziz, P. Kejik, J. Brugger, R.S. Popovic, P. Hoffmann, Appl. Phys. Lett. **86**, 042503 (2005)
42. A. Fernández-Pacheco, J.M.D. Teresa, R. Córdoba, M.R.J. Ibarra, J. Phys. D **42**, 055005 (2009)
43. K. Muthukumar, H.O. Jeschke, R. Valentí, E. Begun, J. Schwenk, F. Porrati, M. Belstein, J. Huth, Nanotech **3**, 546 (2012)
44. Y. Drezner, Y. Greenzweig, D. Fishman, E. van Veldhoven, D.J. Maas, A. Raveh, R.H. Livengood, J. Vac. Sci. Technol. B **30**, 041210 (2012)
45. A.J. DeMarco, J. Melngailis, J. Vac. Sci. Technol. B **19**, 2543 (2001)
46. J.-H. He, P.H. Chang, C.-Y. Chen, K.-T. Tsai, ES Trans. **16**, 13 (2009)
47. M. Prestigiacomo, L. Roussel, A. Houël, P. Sudraud, F. Bedu, D. Tonneau, V. Safarov, H. Dallaporta, Microelectron. Eng. **76**, 175 (2004)
48. I. Utke, T. Bret, D. Laub, P. Buffat, L. Scandella, P. Hoffmann, Microelectron. Eng. **73–74**, 553 (2004)
49. D.C. Joy, A.D. Romig, J. Goldstein, *Principles of Analytical Electron Microscopy* (Springer, Berlin, 1986), p. 270